PHENOMENOLOGICAL MODEL COMBINING DIPOLE-INTERACTION SIGNAL AND BACKGROUND EFFECTS FOR ANALYZING MODULATED DETECTION IN APERTURELESS SCANNING NEAR-FIELD OPTICAL MICROSCOPY

C.-C. Liao and Y.-L. Lo [†]

Department of Mechanical Engineering
National Cheng Kung University
Tainan, Taiwan

Abstract—Modulation methods such as homodyne and heterodyne detections are employed in A-SNOM in order to eliminate serious background effects from scattering fields. Usually, the frequency-modulated detection signal in apertureless scanning near-field optical microscopy (A-SNOM) is generally analyzed using a simple dipole-interaction model based only on the near-field interaction. However, the simulated A-SNOM spectra obtained using such models are in poor agreement with the experimental results since the effects of background signals are ignored. Accordingly, this study proposes a new phenomenological model for analyzing the A-SNOM detection signal in which the effects of both the dipole-interaction and the background fields are taken into account. It is shown that the simulated A-SNOM spectra for 6H-SiC crystal and polymethylmethacrylate (PMMA) samples are in good agreement with the experimental results. The validated phenomenological model is used to identify the experimental A-SNOM parameter settings which minimize the effects of background signals and ensure that the detection signal approaches the pure near-field interaction signal. Finally, the phenomenological model is used to evaluate the effects of the residual stress and strain in a SiC substrate on the corresponding A-SNOM spectrum.

1. INTRODUCTION

Aperture scanning near-field optical microscopy (SNOM) has been proposed as a means of overcoming the inherent resolution limitation of conventional optical microscopy [1]. In SNOM, the illumination light is confined by a metallic aperture patterned on the tip of a tapered metal-coated optical fiber such that a significant enhancement of the near-field effect is obtained. SNOM enables the chemical, structural, and conduction properties of optically scattering media to be obtained at the nanoscale. However, the resolution of SNOM is still restricted by the size of the aperture on the tip of the optical fiber and the waveguide cut-off effect [2]. Furthermore, the very small aperture size used in SNOM severely restricts the light throughput, and therefore reduces the intensity of the detection signal and limits the measurement resolution [3]. Accordingly, an alternative SNOM method known as apertureless scanning near-field optical microscopy (A-SNOM) (or scattering-type SNOM) has been proposed in which the optical fiber is replaced by a sharp vibrating tip. In A-SNOM, the incident light illuminates the tip, thereby producing a small scattering field and inducing a local enhancement of the electric field between the tip and the specimen in the near-field. The localized field enhancement depends on the dipole effect and makes possible an optical resolution at the sub-10 nm scale [4–6].

Although A-SNOM achieves a higher resolution than conventional SNOM, it has a number of practical limitations. For example, the A-SNOM detection signal includes not only the desired near-field interaction field, but also the electric scattering fields produced by the vibrating tip and the sample surface. These scattering fields act as background signals and reduce the precision and reliability of the A-SNOM measurement results. Thus, effective methods are required for eliminating this effect from the detection signal in order to improve the A-SNOM performance.

In A-SNOM, the frequency-modulated detection signal is obtained using either heterodyne [7, 8] or homodyne [8, 9] detection methods. Various models have been proposed for describing the detection signals acquired using the two methods [10–13]. However, these models neglect the detailed background scattering fields. Therefore, in [14, 15], the present group proposed a more straightforward analytical model for analyzing the detection signals obtained in homodyne and heterodyne A-SNOM. The model was used to explore possible strategies for improving the contrast and signal-to-noise ratios in the two detection configurations. Overall, the results showed that heterodyne detection magnifies the near-field signal and obtains a better measurement

performance than homodyne detection as a result. Based on this model, the present group also inserts a superlens in A-SNOM system to improve the whole signal for advanced applications [16].

Although the literature contains various models for describing the A-SNOM detection signal, these models generally fail to distinguish between the tip-sample interaction field and the various background scattering fields. As a result, they provide only qualitative insights into the A-SNOM phenomena. For example, Cvitkovic et al. [17] showed that the conventional quasi-electrostatic point-dipole model provides an adequate qualitative explanation of many A-SNOM phenomena, but does not yield a good quantitative description of the measured near-field contrast. About the dipole effects in near-field, recently some researches have derived the scattering fields from dipole or antenna for different configurations in various conditions, i.e., the analytical models for gold nanorod and ellipsoid illuminated by plane wave polarized along the antenna axis [18], scattering of a plane wave from a perfect electromagnetic conducting (PEMC) elliptic cylinder [19], and the electrostatic potential and field of an electric dipole located in the interface between two dielectric regions [20]. Also, Eroglu and Lee [21] developed the analytical model for radiation from an arbitrarily oriented hertzian dipole in an unbounded electrically gyrotropic medium. These scattering situations from dipole radiation can be analyzed by finite-difference time-domain method (FDTD) [22]. For advanced development, some studies extend the single dipole to dipole antenna array. For example, Zhang et al. [23] proposed a new approach for simultaneously synthesizing the radiation and scattering patterns of linear dipole antenna array, and Laviada-Martinez et al. [24] studied the problem in computing a safety perimeter around the antenna. Accordingly, the authors proposed a new analytical model for the quantitative prediction of material contrasts in scattering-type near-field optical microscopy based upon a modified model of the near-field interaction field. It was shown that the simulated A-SNOM spectra were in better qualitative agreement with the experimental spectra than those obtained using the conventional point-dipole model. However, the modified model fails to accurately reproduce the phonon-polariton resonance spectrum obtained for SiC crystal using the infrared nanoscopy technique proposed in [25]. The limitations of the modified model are due in large part to the omission of the background effects produced by the scattering fields. In other words, the model considers only the interaction electric field between the tip and the sample, and therefore provides only an approximation of the experimental A-SNOM spectra. Consequently, a requirement exists for more sophisticated analytical models in which the effects of both the

tip-sample interaction field and the background scattering fields are taken into account such that quantitative insights into the A-SNOM phenomena can be obtained.

Accordingly, the present study draws upon the various models proposed in [14, 15, 17] and develops a new phenomenological model of the A-SNOM detection signal in which the near-field interaction electric field and the background scattering fields are combined in a single optical interference signal. The validity of the proposed model is demonstrated by comparing the simulated A-SNOM spectra for 6H-SiC crystal and polymethylmethacrylate (PMMA) samples with the experimental results presented in the literature [25, 26]. The model is then used to identify the optimal A-SNOM experimental settings which minimize the effects of background signals such that the detection signal approaches the pure near-field interaction signal. Finally, the practical applicability of the phenomenological model is demonstrated by evaluating the effects of residual stress and strain on the A-SNOM spectra of a SiC sample and comparing the simulation results with those obtained experimentally.

2. PHENOMENOLOGICAL MODEL

Figure 1 presents a schematic illustration of a Mach-Zehnder interferometer-type A-SNOM. As shown, the illuminating light is incident upon a beam splitter (BS), where it is spilt into two beams,
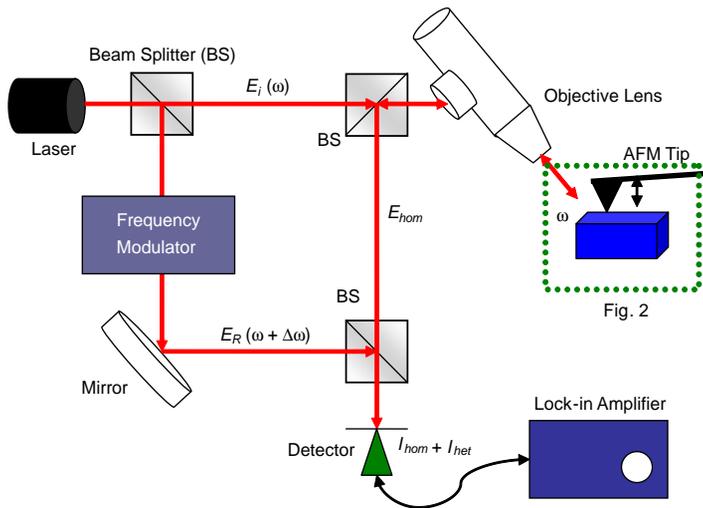

Figure 1. Schematic illustration of heterodyne A-SNOM.

namely the incident beam and the reference beam. The incident electric field, E_i, is passed through an objective lens and focused on the vibrating probe tip of an atomic force microscope (AFM), thereby producing a near-field enhancement effect. The enhancement field and the various scattering electric fields produced within the AFM system are collected by the objective lens and interfere to form the homodyne A-SNOM signal (I_{hom}). Meanwhile, the reference beam is modulated by a frequency modulator such as an acousto-optic modulator (AOM) such that a radian frequency shift, $\Delta\omega$, is added to the frequency of the original beam. In other words, the reference signal incident upon the detector has the form

$$\vec{E}_{Ref} = E_R e^{i[(\omega+\Delta\omega)t+\phi_R]} \tag{1}$$

where ω is the radian frequency of the incident light; and E_R and ϕ_R are the amplitude and phase of the reference beam, respectively. The A-SNOM signal and the reference signal interfere at the detector to produce a heterodyne signal, I_{het}, which is then acquired together with the homodyne signal by a lock-in amplifier.
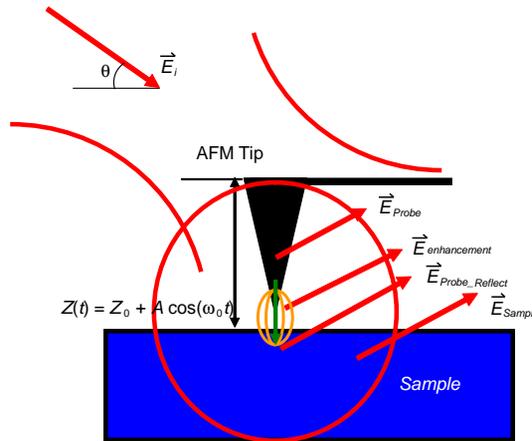
Figure 2. Electric fields in near-field region.

Figure 2 illustrates the electric fields of interest in the near-field region of the AFM system. As shown, the incident field, $\vec{E}_i$, strikes the AFM probe and sample with an angle θ in the focal region and produces four electromagnetic waves, namely (1) an interaction field between the AFM probe tip and the sample, $\vec{E}_{enhancement}$; (2) a scattering field from the AFM probe, $\vec{E}_{Probe}$; (3) a scattering field produced by the vibrating AFM probe and then reflected from the sample surface,

$\vec{E}_{Probe\_Reflect}$; and (4) an electric field scattered directly from the sample surface, $\vec{E}_{Sample}$. Each field is determined by where it is from and which component it is induced by. All the fields can be quantified by properties of materials and formulas from dipole-interaction theory and Fresnel equation. It should be noticed that all fields are related to the incident one, E_i. Therefore, the total intensity collected by the detector can be normalized on the basis of the amplitude of incident field, E_i. The normalization can be employed to make the measured spectra of various materials more distinct.

In developing the phenomenological model of the A-SNOM signal, it is assumed that all four electric fields pass through the objective lens of the AFM system and are incident upon the detector. The AFM drives the probe tip with a vertical sinusoidal vibration around a mean position, Z_0. Assuming that the amplitude and radian frequency of the tip vibration are denoted by A and ω_0, respectively, the dynamic variation of the tip over time can be written as $Z(t) = Z_0 + A\cos(\omega_0 t)$.

In Figure 2, the incident electric field, $\vec{E}_i$, has the form $\vec{E}_i = E_{in}e^{i(\omega t + \phi_{in})}$, where E_{in} is the amplitude, ϕ_{in} is the phase, and ω is the radian frequency. The other electric fields are described in the following items.

(1) Interaction (or enhancement) field

$$\begin{aligned} \vec{E}_{enhancement} &= C \cdot \alpha_{eff}\vec{E}_{in} = C \cdot |\alpha_{eff}|E_{in}e^{i(\omega t + \phi_{\alpha_{eff}} + \phi_{in})} \\ &= C \cdot E_{enhance}e^{i(\omega t + \phi_{enhance})} \end{aligned} \quad (2)$$

where α_{eff} is the effective polarizability; $E_{enhance}$ is the total amplitude of the interaction field; and $\phi_{enhance}$ is the total phase of the interaction field. The interaction field can be multiplied by a specific ratio, C, based on the experimental observation for calibration. According to the general model of quasi-electrostatic theory [7–9], the effective polarizability can be expressed as

$$\alpha_{eff} = \frac{\alpha(1+\beta)}{1 - \frac{\alpha\beta}{16\pi r^3}} \quad \text{with} \quad \alpha = 4\pi a^3\frac{\varepsilon_p - 1}{\varepsilon_p + 2}, \quad \beta = \frac{\varepsilon_s - 1}{\varepsilon_s + 1} \quad (3)$$

where a is the radius of the enhanced dipole (see Figure 3); r is the distance between the dipole and the sample surface; and ε_p and ε_s are the complex dielectric constants of the probe and sample, respectively. Equations (2) and (3) provide a basic insight into the near-field interaction phenomenon in A-SNOM, but fail to adequately reproduce the exactly resonance spectra obtained in practical A-SNOM experiments. Therefore, Cvitkovic et al. [17] proposed a modified
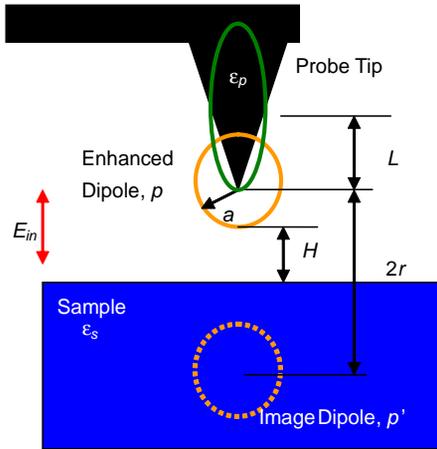
Figure 3. Distribution and location of charges in near-field interaction between AFM probe and sample.

model for the tip-sample interaction field which takes account not only of the size of the probe and the distance between the probe and the sample surface, but also the wavelength of the illuminating light. The modified model presumes that the half-length of the probe, L, must be much shorter than the wavelength of the incident light if the quasi-electrostatic assumption is to hold. As a result, the effective polarizability is re-formulated as follows:

$$\alpha_{eff} = a^2 L \frac{\frac{2L}{a} + \ln \frac{a}{4eL}}{\ln \frac{4L}{e^2}} \left[2 + \frac{\beta \left(g - \frac{a+H}{L} \right) \ln \frac{4L}{4H+3a}}{\ln \frac{4L}{a} - \beta \left(g - \frac{3a+4H}{4L} \right) \ln \frac{2L}{2H+a}} \right] (1 + R_p^2) \quad (4)$$

where L is the half-length of the probe tip, g is a factor related to the proportion of the total induced charge that is relevant for the near-field interaction, and R_p is the Fresnel reflection coefficient for p-polarized light.

Since the amplitude of the interaction electric field is nonlinear, the $E_{enhance}$ term in Equation (2) can be approximated as the sum of the individual components oscillating at different harmonics, $n\omega_0$, of the AFM probe modulation radian frequency [9]. In other words, $E_{enhance}$ can be expressed as [27]

$$
\begin{aligned}
E_{enhance} &= E_{enhance}^{0\omega_0} + E_{enhance}^{1\omega_0} \cos(\omega_0 t) + E_{enhance}^{2\omega_0} \cos(2\omega_0 t) \\
&\quad + E_{enhance}^{3\omega_0} \cos(3\omega_0 t) + \ldots \\
&= \sum_{n=0}^{\infty} E_{enhance}^{n\omega_0} \cos(n\omega_0 t)
\end{aligned}
\quad (5)
$$

where the series coefficients, $E_{enhance}^{n\omega_0}$, can be obtained from the Fourier components of $\alpha_{eff}E_{in}$. Note that the ratio of the Fourier components differs depending on the interaction model used (e.g., Equation (3) or Equation (4)).

(2) Scattering field from probe

$$\vec{E}_{Probe} = E_P e^{i(\omega t + \phi_P)} e^{i[2k\sin(\theta)Z(t)]} \tag{6}$$

where $E_P = R_{Probe}E_{in}$ is the amplitude of the scattering field and is related to the reflective coefficient of the probe, R_{probe}, that can be determined according to Fresnel equation for p polarization (the incident angle equals to θ and the light is from air to probe); k is the wave number of the incident light and given by $2\pi/\lambda$; and $e^{i[2k\sin(\theta)Z(t)]}$ is the phase vibration caused by the vertical dither of the probe. The total phase of the scattering field from the probe, $\phi_P = \phi_{Probe\_initial} + \phi_{R_{probe}} + \phi_{in}$, is the sum of various factors including the initial phase relative to the probe ($\phi_{Probe\_initial}$), the phase caused by the factor in the probe reflective coefficient ($\phi_{R_{probe}}$), and the phase from the incident light (ϕ_{in}). Importantly, the probe tip scattering fields produced by the incident light directly and by the incident light reflected from the sample onto the tip, respectively, both have a phase $2k\sin(\theta)Z(t)$ and a radian frequency, ω. Thus, the two scattering fields can be treated as a single field for the sake of simplicity.

(3) Scattering field produced by vibrating AFM probe and then reflected from sample surface

$$\begin{aligned}\vec{E}_{Probe\_Reflect} &= E_{P\_R} e^{i[2k\sin(\theta)Z(t)]} e^{i(\omega t + \phi_{P\_R})} e^{i[2k\sin(\theta)Z(t)]} \\ &= E_{P\_R} e^{i(\omega t + \phi_{P\_R})} e^{i[4k\sin(\theta)Z(t)]}\end{aligned} \tag{7}$$

where $E_{P\_R} = R_{Sample}E_P = R_{Sample}R_{Probe}E_{in}$ is the amplitude determined by the reflective coefficients of the probe and sample, respectively. R_{sample} can be calculated according to Fresnel equation for p polarization (the incident angle equals to $\pi/2 - \theta$ and the light is from air to sample). The total phase of the scattering field, $\phi_{P\_R} = \phi_{Sample\_initial} + \phi_{R_{Sample}} + \phi_{Probe\_initial} + \phi_{R_{Probe}} + \phi_{in}$, is the sum of various factors including the initial phase relative to the sample and probe ($\phi_{Sample\_initial}$, $\phi_{Probe\_initial}$), the phase caused by the factors in the probe and sample reflective coefficients ($\phi_{R_{Sample}}$, $\phi_{R_{Probe}}$), and the phase from the incident field (ϕ_{in}). From Figure 2, the optical path difference between the field scattered by the probe directly and that scattered by the probe and then reflected by the sample surface

is equal to $2k\sin(\theta)Z(t)$. Therefore, the phase relative to the path between the probe and the sample surface is given by $4k\sin(\theta)Z(t)$.

(4) Scattering field from sample surface

$$\vec{E}_{Sample} = E_S e^{i(\omega t + \phi_S)} \tag{8}$$

where $E_S = R_{Sample}E_{in}$ is the amplitude of the scattered field and is determined by the reflective coefficient of the sample. The total phase of the scattered field from sample, $\phi_S = \phi_{Sample\_initial} + \phi_{R_{Sample}} + \phi_{in}$, is the sum of various factors including the initial phases relative to the sample ($\phi_{Sample\_initial}$), the phase caused by the factor in the sample reflective coefficient ($\phi_{R_{Sample}}$), and the phase from the incident field (ϕ_{in}).

The most important fields induced by the incident light and scattering from main components of AFM are described as above. The other possible scattering fields can be integrated into these four fields or be neglected. For example, the scattering field from sample surface and then reflected from probe has the same formula as Equation (7), which means it can be simplified and combined with the main fields. Also, the other multi-scattering fields may be too weak to be detected or scatter out of the range in the focal region of objective lens, and hence they can be neglected. As shown in Figure 1, the total electric field coupled into the detector is equivalent to the sum of the four electric fields produced in the near-field region of the AFM system and the reference signal, i.e.,

$$\vec{E}_{total} = \vec{E}_{enhancement} + \vec{E}_{Probe} + \vec{E}_{Probe\_Reflect} + \vec{E}_{Sample} + \vec{E}_{Ref} \tag{9}$$

The total intensity signal is given by the sum of the homodyne and heterodyne signals, i.e.,

$$I_{total} = I_{hom} + I_{het} \tag{10}$$

where the homodyne signal, I_{hom}, contains the four fields which interfere in the near-field region of the AFM system and are collected by the objective lens, while the heterodyne signal, I_{het}, contains the field produced by the interference between the modulated reference signal and the four near-field signals.

It was shown in [15, 28], that the heterodyne detection technique provides a better A-SNOM performance than the homodyne detection method. Therefore, the phenomenological model proposed in this study is based on the heterodyne detection signal. Hence, the amplitude and phase of the reference beam E_R are key factors in the phenomenological model. The intensity of the heterodyne modulated signal in the form of a Bessel function and rearranging in accordance

with the order of the modulation radian frequency, i.e., $\Delta\omega + n\omega_0$, the heterodyne intensity signal can be obtained as the sum of the individual harmonic modulation orders [14, 15, 29], i.e.,
$\Delta\omega t$ term:

$$2C \cdot E_{enhance}^{0\omega_0} E_R \cos(\Delta\omega t + \phi_R - \phi_{enhance}) + 2E_S E_R \cos(\Delta\omega t + \phi_R - \phi_S)$$
$$+ 2E_P E_R J_0(\varphi_3) \cos(\Delta\omega t + \varphi_1) + 2E_{P\_R} E_R J_0(2\varphi_3) \cos(\Delta\omega t + \varphi_2) \quad (11)$$

$\Delta\omega t + 1\omega_0 t$ term for the first order harmonic modulation:

$$2C \cdot E_{enhance}^{1\omega_0} E_R \cos(\omega_0 t) \cos(\Delta\omega t + \phi_R - \phi_{enhance})$$
$$+ 4E_P E_R J_1(\varphi_3) \cos(\omega_0 t) \sin(\Delta\omega t + \varphi_1)$$
$$+ 4E_{P\_R} E_R J_1(2\varphi_3) \cos(\omega_0 t) \sin(\Delta\omega t + \varphi_2) \quad (12)$$

$\Delta\omega t + 2\omega_0 t$ term for the second order harmonic modulation:

$$2C \cdot E_{enhance}^{2\omega_0} E_R \cos(2\omega_0 t) \cos(\Delta\omega t + \phi_R - \phi_{enhance})$$
$$- 4E_P E_R J_2(\varphi_3) \cos(2\omega_0 t) \cos(\Delta\omega t + \varphi_1)$$
$$- 4E_{P\_R} E_R J_2(2\varphi_3) \cos(2\omega_0 t) \cos(\Delta\omega t + \varphi_2) \quad (13)$$

$\Delta\omega t + 3\omega_0 t$ term for the third order harmonic modulation:

$$2C \cdot E_{enhance}^{3\omega_0} E_R \cos(3\omega_0 t) \cos(\Delta\omega t + \phi_R - \phi_{enhance})$$
$$- 4E_P E_R J_3(\varphi_3) \cos(3\omega_0 t) \sin(\Delta\omega t + \varphi_1)$$
$$- 4E_{P\_R} E_R J_3(2\varphi_3) \cos(3\omega_0 t) \sin(\Delta\omega t + \varphi_2) \quad (14)$$

$\Delta\omega t + 4\omega_0 t$ term for the fourth order harmonic modulation:

$$2C \cdot E_{enhance}^{4\omega_0} E_R \cos(4\omega_0 t) \cos(\Delta\omega t + \phi_R - \phi_{enhance})$$
$$+ 4E_P E_R J_4(\varphi_3) \cos(4\omega_0 t) \cos(\Delta\omega t + \varphi_1)$$
$$+ 4E_{P\_R} E_R J_4(2\varphi_3) \cos(4\omega_0 t) \cos(\Delta\omega t + \varphi_2) \quad (15)$$

where $\varphi_1 = \phi_R - \phi_P - 2k\sin(\theta)Z_0$, $\varphi_2 = \phi_R + \phi_{P\_R} - 4k\sin(\theta)Z_0$, and $\varphi_3 = 2k\sin(\theta)A$. The formulations given in Equations (11) sim (15) enable the near-field phenomena observed in the A-SNOM system to be analyzed for the first four harmonic orders of the modulation frequency, i.e., $\Delta\omega t + \omega_0 t$ to $\Delta\omega t + 4\omega_0 t$. However, the formulations can be easily extended to analyze the A-SNOM phenomena at higher harmonics if required.

3. VALIDATION OF PHENOMENOLOGICAL MODEL

In this section, the validity of the phenomenological model is confirmed by comparing the simulation results obtained for the first four harmonic orders of the modulated heterodyne detection signal for two illustrative samples with the experimental results presented in the literature [25, 26].

The incident light passes through an objective lens, focuses on a sphere region as shown in Figure 2 and induces some scattering fields. Since the scattering fields shown as Equations (6) to (8) are in the same near-field region, it can be assumed that they have similar order in magnitude. According to the illuminated area of the AFM probe and the sample in the focal region, the scattering fields from the sample, E_S, from the probe, E_P, and from the probe and then reflected from sample, E_{P_R}, should be multiplied by a ratio set as 1:0.5:0.1. Therefore, the constant ratios among scattering fields in the simulation is equivalent to $E_S : 0.5 \ E_P : 0.1 \ E_{P\_R} = R_{Sample}E_{in} : 0.5$ $R_{Probe}E_{in} : 0.1 \ R_{Sample}R_{Probe}E_{in}$. Due to these fields are all induced by the incident light, the measured spectra can be normalized and calculated on the basis of the amplitude of incident field, E_{in}. It should be noticed that since different measurements in different materials are discussed, each electric field induced by the incident one will be related to the reflective coefficient of the material. The phase of each electric field also should be considered carefully according to the relative locations of the components in the AFM in order to correspond to the actual experimental condition. All the considered fields are listed above [14, 15]. Their amplitudes and phases will be relative to the reflective and scattering coefficients and states of components in near-field region, and are determined as functions of the radian frequency. Additionally, the amplitude of the reference signal, E_R is set as 1, and phase, ϕ_R, can be determined as $\pi/2$ in order to avoid the phase ambiguity in A-SNOM interferometric signal.

In [25], the authors used A-SNOM to measure the near-field optical phonon-polariton resonance spectrum of 6H-SiC crystal. The platinum-coated tip of the AFM used to carry out the measurements had an apex of $\sim 20\,\text{nm}$ and was illuminated by infrared light with frequencies ranging from $880 \sim 1090\,\text{cm}^{-1}$. The tip vibrated vertically with an amplitude of around $20 \sim 30\,\text{nm}$ at a frequency of approximately $300\,\text{kHz}$. Interferometric detection of the backscattered light and the subsequent demodulation of the detection signal were performed at the second harmonic of the tapping frequency.

In simulating the phonon-polariton resonance spectrum of the 6H-SiC sample, it is assumed that the amplitude of the $n\omega_0$ components of the enhancement electric field is given by $E_{enhance}^{n\omega_0} \propto$ $E_{enhance} \propto \alpha_{eff}E_{in}$. Thus, the variation of $E_{enhance}^{n\omega_0}$ with the tip-to-sample distance, Z_0, can be simulated directly using the effective polarizability formulae given in Equation (3) (conventional tip-sample interaction model [7–9]) or Equation (4) (modified tip-sample interaction model [17]). In the present example, the wavelength of the illuminating light is approximately $10\,\mu\text{m}$, and is therefore much

longer than the half-length of the tip, $\sim 300\,\text{nm}$. Thus, the tip-sample interaction field is simulated using the modified model given in Equation (4). The amplitude of the tip vibration, A, and the parameter, H, in Equation (4) can be both set as $25\,\text{nm}$ [25]. Since the resolution of A-SNOM based on the size of the near-field interaction dipole [4–6] is around $10\,\text{nm}$, the radius of the interaction sphere, a, can be determined as $10\,\text{nm}$. According to [17], the factor g related to the proportion of the total induced charge that is relevant for the near-field interaction can be estimated as 0.7 ± 0.1. However, in practice, g is a complex factor with an imaginary component induced by whose value depends on the phase difference amongst the driving field, the response of the enhancement, and the other participative fields. In other words, parameters g and L in Equation (4) vary depending on the particular experimental setup. In accordance with the experimental system used in [25], the present simulations specify g and L as $0.75e^{0.52i}$ and $300\,\text{nm}$, respectively. It should be noted that the incident angle of the reflective coefficient, R_p, in the modified interaction model (Equation (4)) is different from that of the incident light in the scattering field formulations given in Equations (6) $\sim$ (8). In accordance with [17], the simulations specify R_p as 90 degrees. Meanwhile, the incident angle of the illuminating light is specified as $30°$ in accordance with the recommendations given in [30]. The dielectric constants of materials employed in A-SNOM system can be referred to Table 1. In Equation (2), the constant ratio, C, for the interaction field related to SiC is considered in order to reasonably interfere with other scattering fields. Thus, C can be adjusted as 2×10^{19} by the observation on the relative harmonic modulation signals in different orders. This value is also acceptable according to the simulation in dipole-interaction fields in Ref. [9].

Figure 4 compares the simulation and experimental results for the polariton-resonance spectrum of the 6H-SiC crystal sample. The measured spectrum of the experiment shown as a least-squares fit to the experimental data points can be found in Figure 1(c) of Ref. [25]. The simulated and experimental results for the 2nd order harmonic detection signal are normalized according to each maximum value and shown by the black solid line and the blue dashed line, respectively, while the simulation results for the 1st and 3rd order harmonic detection signals are shown by the red and orange solid lines, respectively. It is observed that a good agreement exists between the 2nd order harmonic detection signal simulated using the proposed phenomenological model and the experimental detection signal reported in [25]. The figure also shows the results obtained for the detection signal when using the pure interaction model proposed

Table 1. Properties of Materials in A-SNOM.

|	**Model of dielectric constant, ε**	**Values in model**
Pt-coated tip [31]	$(n - ik)^2$	$n = 9.91$, $k = 36.7$ for $\omega \sim 1049$ cm^{-1} $n = 5.24$, $k = 21.5$ for $\omega \sim 1774$ cm^{-1}
6H-SiC [32]	$\varepsilon_\infty\left[1 + \dfrac{\omega_L^2 - \omega_T^2}{\omega_T^2 - \omega^2 - i\omega\Gamma} - \dfrac{\omega_p^2}{\omega(\omega + i\gamma)}\right]$	$\varepsilon_\infty = 6.7$, $\omega_L = 964.2$, $\omega_T = 788$, $\omega_p = 70$, $\Gamma = 5.2$, $\gamma = 110$ Unit: cm^{-1}
PMMA [26]	$\operatorname{Re}[\varepsilon_{PMMA}] + i\operatorname{Im}[\varepsilon_{PMMA}]$	
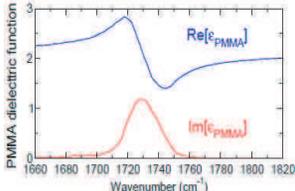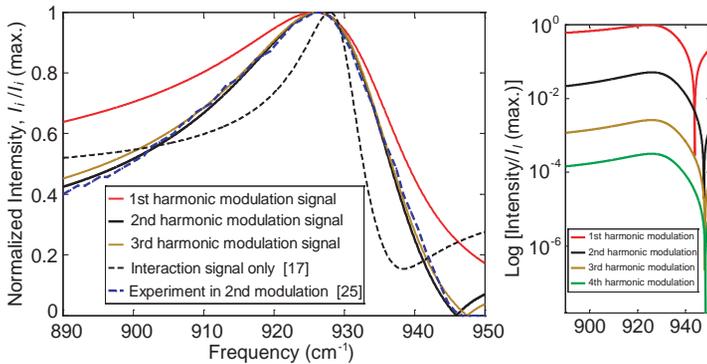
Figure 4. Comparison of simulated and experimental modulated heterodyne detection signals for 6H-SiC crystal sample. The right side of the figure shows the intensity of different harmonic modulations relative to that of 1st harmonic modulation.

in [17], in which the effects of background effects are ignored. It can be seen that the simulated detection signal deviates notably from the experimental signal. Thus, it can be inferred that in attempting to accurately reproduce the experimental modulated A-SNOM detection signal, the background scattering fields must be taken into account (i.e., as in the phenomenological model proposed in this study). The relative intensities of these different harmonic modulation signals are also shown at the right side of the figure. It shows that the detected

intensity decays rapidly at higher harmonic modulation. Although the signal can be extracted more precisely [7–9] at the higher harmonic modulations, these signals may be too weak to be detected. Therefore, most experiments are conducted in measuring the 2nd or 3rd harmonic modulation signal.

The validity of the proposed phenomenological model was further evaluated by comparing the simulated detection signal for a polymethylmethacrylate (PMMA) sample with the experimental results presented in [26]. The simulations replicated the experimental setup used in [26], namely (1) a Pt-coated tip oscillating at its resonance frequency of $\sim 35\,\mathrm{kHz}$ with a tapping amplitude of $50\,\mathrm{nm}$, which means the amplitude of the tip vibration, A, and the parameter, H, in Equation (4) can be both set as $50\,\mathrm{nm}$; (2) a mid-infrared CO-laser source with frequencies in the range $1680 \sim 1800\,\mathrm{cm}^{-1}$. Since the wavelength of the incident light is much longer than the half-length of the vibrating tip, the simulations once again used the modified tip-sample interaction model given in Equation (4). Since the resolution of A-SNOM based on the size of the near-field interaction dipole [4–6] is around $10\,\mathrm{nm}$, the radius of the interaction sphere, a can be determined as $10\,\mathrm{nm}$. Also, the dielectric constants of materials employed in A-SNOM system can be referred to Table 1. In accordance with the experimental setup in [26], parameters g and L in the interaction model were specified as $g = 3e^{0.45i}$ and $L = 300\,\mathrm{nm}$, respectively. Note the constant ratio, C, for the interaction field related to PMMA in Equation (2) is considered and adjusted as 0.8×10^{19} by the observation on the relative harmonic modulation signals in different orders. This value is also acceptable according to the simulation in dipole-interaction fields in [9]. In [26], interferometric detection of the backscattered light, and the subsequent demodulation of the detection signal, were performed at the third harmonic of the tapping frequency. However, in the simulations, the detection signal was synthesized for the first four harmonic orders of the modulated frequency in order to enable a more thorough comparison to be made between the experimental and simulation results.

Figure 5 compares the simulation and experimental results for the modulated heterodyne detection signal of the PMMA sample. The experimental detection signal is shown by the dashed blue line, while the corresponding simulated signal is shown by the solid orange line. Meanwhile, the simulation results for the 1st and 2nd order harmonic modulated detection signals are shown by the solid red and black lines, respectively. As expected, the simulated detection signal obtained using the pure interaction model deviates significantly from the experimental detection signal since the effects of background signals
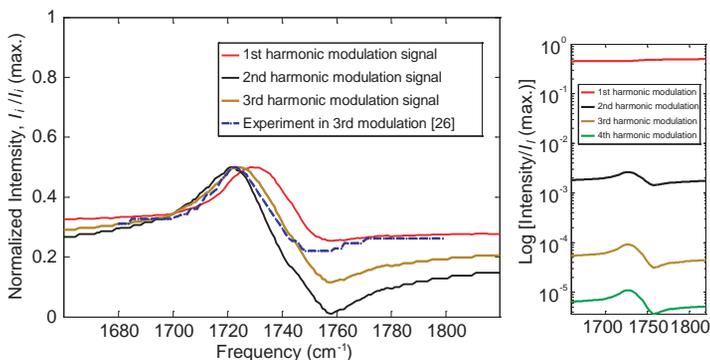
Figure 5. Comparison of simulated and experimental modulated heterodyne detection signals for PMMA sample. The right side of the figure shows the intensity of different harmonic modulations relative to that of 1st harmonic modulation.

are neglected. By contrast, the simulation results obtained using the proposed phenomenological model for the 3rd order harmonic of the detection signal are in far better agreement with the experimental signal. However, it is noted that the fit between the simulated and experimental detection signals is not as good as that shown in Figure 3 for the 6H-SiC sample. The relatively poorer performance of the phenomenological model in the current example can be attributed to two main factors. Firstly, some of the experimental conditions in [26] are inconsistent with the assumptions made in the modified tip-sample interaction model [17]. For example, the wavelength of the incident light used in [26] was not constant, but varied in the range $6 \sim 10 \, \mu m$. As a result, the constant parameter settings of g and L used in the simulations do not accurately reproduce the actual experimental values. Secondly, in [26], the demodulation of the detection signal was performed at the third harmonic of the tapping frequency rather than the second harmonic, i.e., as in [25]. As a result, the whole detection signal contains a greater amount of background effects and needs to be demodulated by higher order harmonic frequency. Thus, it is possible that the detection signal is affected by unexpected noise fields which are not considered in the phenomenological model. Nonetheless, the good qualitative agreement between the simulated 3rd and 4th order harmonic detection signals and the experimental signal confirms the basic validity of the proposed phenomenological model.

4. ELIMINATION OF BACKGROUND EFFECTS IN A-SNOM DETECTION SIGNAL

In setting up an A-SNOM system, the objective is to minimize the background effects such that the detection signal approaches the pure near-field interaction signal (i.e., E_{hance} in Equations (11) $\sim$ (15). The previous section has confirmed the basic validity of the phenomenological model proposed in this study. Accordingly, in this section of the paper, the model is used to explore the effects of various A-SNOM parameters on the detection signal in order to identify the experimental configuration which suppresses the background effects and yields the pure near-field interaction signal.

Figure 6 illustrates the detection signals (1st $\sim$ 4th harmonic orders) obtained using the proposed phenomenological model for various values of the incident wavelength, incident angle and tip
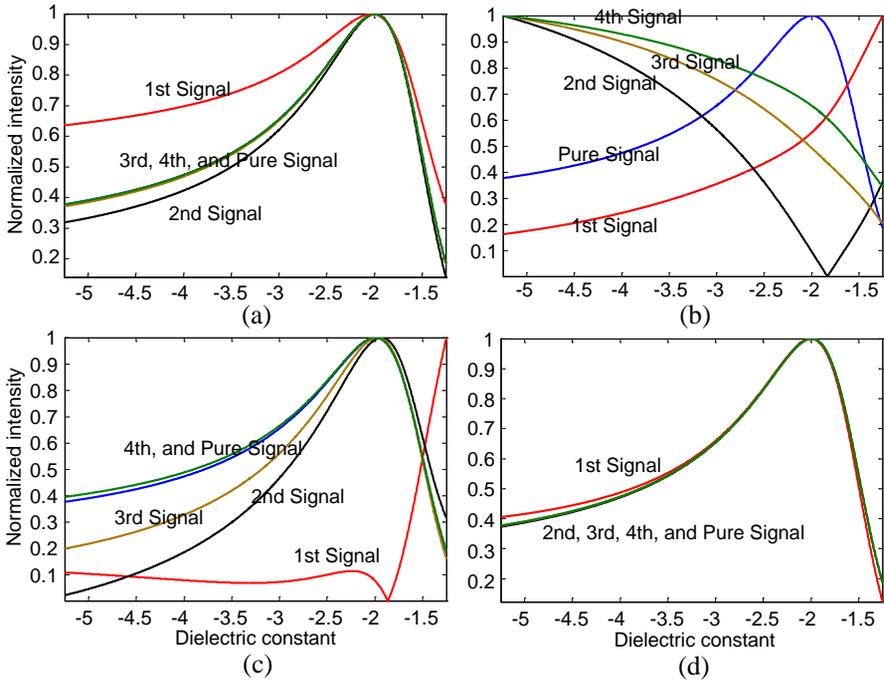
Figure 6. Simulated A-SNOM spectra for various experimental configurations: (a) $\lambda = 10\,\mu\text{m}$, $\theta = 30°$, $A = 30\,\text{nm}$; (b) $\lambda = 633\,\text{nm}$, $\theta = 30°$, $A = 30\,\text{nm}$; (c) $\lambda = 633\,\text{nm}$, $\theta = 30°$, $A = 5\,\text{nm}$; (d) $\lambda = 633\,\text{nm}$, $\theta = 5°$, $A = 5\,\text{nm}$. (Note that the tip-sample interaction is modeled using Equation (4)).

vibrational amplitude. Note that the remaining A-SNOM parameters (e.g., radius of tip, length of probe, distance between tip and sample, and so on) are assigned in accordance with the experimental conditions used in [25]. The pure near-field interaction signal obtained using the phenomenological model and only related to desired $E_{enhance}$ is also presented for comparison purposes. In every case, the modulated detection signals are simulated for dielectric constants ranging from $-5 \sim -1.5$ since these values approximate the dielectric constant of SiC at the frequencies considered in [25], i.e., $880\,\mathrm{cm}^{-1}$ to $1090\,\mathrm{cm}^{-1}$. Figure 6(a) presents the simulation results obtained for an incident wavelength of $10\,\mu\mathrm{m}$, an incident angle of $30°$, and a tip vibrational amplitude of $30\,\mathrm{nm}$. It can be seen that 3rd and 4th order harmonic modulation detection signals virtually overlap the near-field interaction signal. In order words, the results substantiate the claim in [9, 14, 15] that the higher order harmonic modulation detection signals are more robust toward the effects of background signals and are therefore in better agreement with the pure interaction signal.

The qualitative observations presented in [9] showed that the signal contrast in an A-SNOM system can be improved by using light with a longer wavelength. In Figure 6(b), this claim is investigated by reducing the incident wavelength to $633\,\mathrm{nm}$ (i.e., within the visible light range) with the expectation that the background effects will cause the modulated detection signals to deviate notably from the pure interaction signal. Note that the incident angle and tip vibrational amplitude are assigned the same values as those used in Figure 6(a). The results presented in Figure 6(b) show that all of the detection signals deviate significantly from the pure interaction signal. Thus, the simulation results confirm the suitability of using long-wavelength light such as infrared light as the illumination source for A-SNOM applications.

It was shown in [7–9, 14, 15] that when performing A-SNOM using visible light with a wavelength of around $633\,\mathrm{nm}$, the effects of background signals can be suppressed by reducing the modulation depth relative to the effect of the tip vibrational amplitude, the angle of the incident light, and so on. Figure 6(c) shows the simulation results obtained for the A-SNOM detection signal given an incident wavelength of $633\,\mathrm{nm}$, an incident angle of $30°$, and a tip vibrational amplitude of $5\,\mathrm{nm}$. In contrast to the results presented in Figure 6(b) for a tip vibration amplitude of $30\,\mathrm{nm}$, it can be seen that the 3rd order harmonic modulated signal approaches the pure interaction signal, while the 4th order harmonic modulated signal virtually overlaps the pure interaction signal. In other words, the results confirm that a lower modulation depth provides an effective means of suppressing the effects

of background signals when performing A-SNOM using visible light.

Figure 6(d) presents the simulation results obtained for the detection signal when the incident wavelength is specified as 633 nm, the tip vibrational amplitude is assigned a value of 5 nm, and the incident angle is reduced to 5°. In this case, it is observed that the 2nd $\sim$ 4th order harmonic modulated signals are in very close agreement with the pure interaction signal. Thus, the results confirm the findings in [7–9, 14, 15] that a smaller incident angle suppresses the background effects when using visible light as the illuminating source for A-SNOM, and therefore causes the detection signal to approach the desired pure near-field interaction signal.

Overall, the results presented in Figure 6 show that the proposed phenomenological model provides a convenient means of predicting the A-SNOM spectra for various experimental configurations. As a result, the model enables the experimental A-SNOM configuration to be tuned in advance in such a way as to optimize the detection signal without the need for an expensive and time-consuming trial-and-error adjustment process.

In A-SNOM, the detection signal is seriously degraded by background signals at lower harmonic orders of the modulation frequency. However, the modulated signal obtained when the illuminating frequency is close to that of the resonance frequency approaches the pure near-field interaction signal. That is, the relative effects of the background signals on the detection signal are reduced. Thus, by simulating the phonon-polariton resonance spectrum of a material using the proposed phenomenological model, the resonance frequency of the material can be predicted simply by inspecting the low order harmonic detection signal and identifying the frequency at which the signal obtains its maximum value. The identified frequency can then be used as the experimental illumination frequency, thereby suppressing the effects of background signals on the detection signal and improving the measurement performance as a result.

In contrast to existing analytical A-SNOM models, the phenomenological model proposed in this study takes account not only of the pure tip-sample interaction field, but also the effects of the background signals produced by the various scattering fields in the near-field region of the AFM system. In the preceding simulations, the tip-sample interaction field was modeled using the modified formulation given in Equation (4) since the wavelength of the illuminating light is much longer than the half-length of the probe tip. In practice, however, the choice of a suitable tip-sample interaction model depends on the particular A-SNOM configuration. Significantly, the phenomenological model proposed in this study can simulate the

interaction field using any existing dipole-interaction formulation (e.g., those given in Equations (3) and (4), or indeed any new formulation which may be developed in the future. In other words, it provides a robust and versatile means of analyzing and explaining the A-SNOM detection signal.

Figure 7 presents the simulation results obtained by the phenomenological model for the first four harmonic orders of the modulated detection signal for the SiC sample when modeling the tip-sample interaction field using the conventional quasi-electrostatic model given in Equation (3). In Figure 7(a), the experimental conditions are identical to those used in Figure 6(a), and a good agreement is again obtained between the 3rd and 4th order harmonic modulated signals and the pure interaction signal. Figure 7(b) considers the same experimental conditions as those used in Figure 6(b), and again shows that all of the detection signals deviate
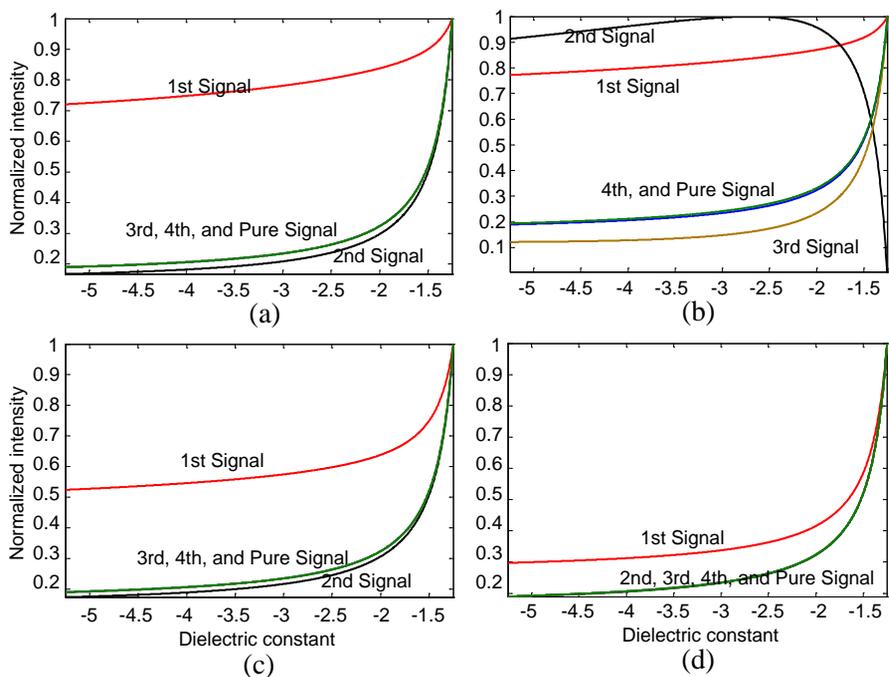
Figure 7. Simulated A-SNOM spectra for various experimental configurations: (a) $\lambda = 10\,\mu\text{m}$, $\theta = 30°$, $A = 30\,\text{nm}$; (b) $\lambda = 633\,\text{nm}$, $\theta = 30°$, $A = 30\,\text{nm}$; (c) $\lambda = 633\,\text{nm}$, $\theta = 30°$, $A = 5\,\text{nm}$; (d) $\lambda = 633\,\text{nm}$, $\theta = 5°$, $A = 5\,\text{nm}$. (Note that the tip-sample interaction is modeled using Equation (3)).

notably from the pure interaction signal. The simulation parameters used in Figure 7(c) reproduce those used in Figure 6(c). It is again found that the simulated 3rd order harmonic modulated signal is in close agreement with the pure interaction signal. Finally, Figure 7(d) uses the same experimental parameters as those considered in Figure 6(d), and shows that a close agreement is obtained between the 2nd $\sim$ 4th order harmonic modulated detection signals and the pure interaction signal. In other words, for all four sets of experimental conditions, the results obtained by the phenomenological model using the conventional dipole-interaction model (Equation (3)) are consistent with those obtained using the modified interaction model (Equation (4)).

## 5. APPLICATION OF PHENOMENOLOGICAL MODEL TO RESIDUAL STRESS AND STRAIN MEASUREMENT

Silicon carbide (SiC) crystal is one of the most robust semiconductor materials. However, the manufacturing process invariably induces a residual stress (or strain) within SiC components, which degrades their mechanical and electrical performance and potentially reduces their service lives. As a result, a requirement exists for methods capable of measuring the local stress and strain within SiC components such that the fabrication process can be optimized and the performance of the components correspondingly improved. A-SNOM enables the nanoscale properties of a material to be determined in a non-invasive manner and requires no particular sample preparation process. As a result, A-SNOM provides an attractive means of obtaining local stress and strain measurements. The results presented in Section 3 have demonstrated the ability of the proposed phenomenological model to accurately predict the phonon-polariton resonance spectrum of 6H-SiC crystal (see Figure 4). In the present section, a method is proposed for using the phenomenological model to evaluate the effects of residual stress or strain on the A-SNOM spectrum of a SiC sample.

In A-SNOM, the detection signal is directly related to the dielectric constant of the sample. The dielectric constant of SiC can be expressed as a function of the frequency using the following classical damped harmonic oscillator model [31]:

$$\varepsilon(\omega) = \varepsilon_\infty \left(1 + \frac{\omega_{LO}^2 - \omega_{TO}^2}{\omega_{TO}^2 - \omega^2 + i\Gamma\omega} \right) \tag{16}$$

where ω_{LO} and ω_{TO} are the longitudinal and transverse optical phonon frequencies, respectively. ε_∞ is the high-frequency dielectric constant, and Γ describes the phonon damping of the corresponding mode.

In [25], it was shown that the presence of stress or strain within the A-SNOM sample results in a line shift of the longitudinal optical phonon-frequencies. In Figure 8, the solid black line shows the frequency response of an unstrained SiC sample. From inspection, the maximum intensity of the detection signal occurs at a frequency of $\omega_{sp} = 927 \, \text{cm}^{-1}$. In the case of a strained sample, the spectrum is shifted by a distance $\Delta\omega$ relative to that of the unstrained sample. Note that ω_{sp} approximates ω_{LO} in Equation (16), and thus $\Delta\omega \approx \Delta\omega_{LO}$ [33]. Since the shift in the longitudinal optical phonon-frequency is directly related to the magnitude of the stress or strain in the SiC sample [34], the intensity of the stress or strain can be estimated simply by measuring the corresponding shift in the A-SNOM spectrum.
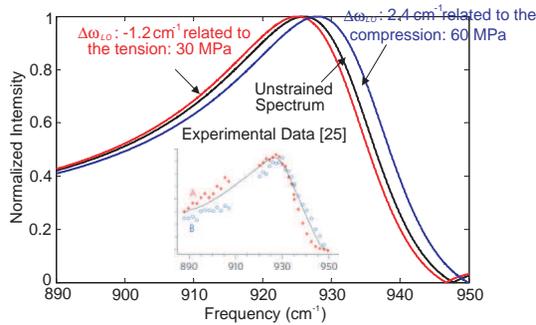
Figure 8. Simulated A-SNOM spectra for SiC sample with regions of residual stress. The black line represents the spectrum of the unstrained SiC sample (reproduced directly from Figure 4). The red line represents the spectrum of the region of the SiC sample with a tensile stress of $30 \, \text{MPa}$ and $\Delta\omega_{LO} - 1.2 \, \text{cm}^{-1}$. The blue line represents the spectrum of the region of the SiC sample with a compressive stress of $60 \, \text{MPa}$ and $\Delta\omega_{LO} \sim 2.4 \, \text{cm}^{-1}$.

In the experiments performed in [25], the sample contained a region of tensile stress with a magnitude of $30 \, \text{MPa}$ and a region of compressive stress with a magnitude of $60 \, \text{MPa}$. The corresponding frequency shifts in the A-SNOM spectrum were found to be $\Delta\omega \sim -1.2 \, \text{cm}^{-1}$ and $\Delta\omega \sim +2.4 \, \text{cm}^{-1}$, respectively. According to the estimation of the frequency shift related to the residual stress and strain, the shift of the longitudinal optical phonon frequency, $\Delta\omega_{LO}$ in dielectric function of SiC (the change of ω_{LO} in Equation (16)) can be found. Using these values to approximate the change of ω_{LO} in Equation (16), Figure 8 shows the simulation results obtained by the phenomenological model for the A-SNOM spectra of the tension and compression regions of the SiC sample.

From inspection, the spectrum associated with the tension region of the SiC sample (i.e., the red line) has a peak value at a frequency of $\sim 926\,\mathrm{cm}^{-1}$, while the spectrum associated with the compression region of the SiC sample (i.e., the blue line) has a peak value of $\sim 928\,\mathrm{cm}^{-1}$. These results are in reasonable agreement with the experimental data presented in [25]. Hence, the proposed model provides a convenient means of predicting the effects of residual stress and strain on the corresponding A-SNOM spectrum. Furthermore, it can be inferred that the proposed model enables the unknown local complex dielectric function of a material to be extracted from the measured A-SNOM spectra of the material.

6. CONCLUSIONS

Most existing analytical models of the A-SNOM detection signal consider only the dipole-interaction field, i.e., the effects of background signals are ignored. As a result, a poor agreement is obtained between the simulated A-SNOM spectra and the corresponding experimental spectra. Consequently, this study has proposed a phenomenological model for the A-SNOM detection signal in which both the tip-sample interaction field and the various scattering electric fields in the near-field region are taken into account. The model enables the heterodyne detection signal to be simulated at any harmonic order of the modulation frequency. It has been shown that the simulated A-SNOM spectra for 6H-SiC and PMMA are in good agreement with the experimental results presented in the literature [25, 26].

The proposed model not only provides the means to simulate the A-SNOM spectra of a sample, but also enables the effects of the various experimental A-SNOM parameter settings to be systematically explored such that the experimental A-SNOM system can be configured in such a way as to minimize the effects of the background signals. In other words, the model provides the ability to tune the A-SNOM configuration in advance without the need for a time-consuming trial-and-error adjustment process. The simulation results have confirmed the experimental findings in [8, 9, 14, 15] that the detection signal approaches the desired pure near-field signal when the modulation order is increased, the angle of incidence of the illumination light is reduced, the wavelength of the illumination light is increased, and the modulation depth is reduced.

The literature contains various dipole-interaction models for simulating the near-field interaction signal in A-SNOM, including the conventional quasi-electrostatic model [7–9] and the modified model [17]. In practice, the choice of an appropriate model

depends on the particular A-SNOM configuration. However, the simulation results presented in this study have shown that the proposed phenomenological model accurately reproduces the experimental A-SNOM spectra irrespective of the dipole-interaction model applied. Hence, it can be utilized as a tool for advanced applications in measurement. In other words, the proposed model not only provides a robust and versatile approach for modeling the detection signals obtained using existing tip-sample interaction models, but can also be reasonably expected to reproduce the detection signals obtained using any new tip-sample interaction models developed in the future.

Finally, it has been shown that the simulated A-SNOM spectra obtained by the proposed model for a sample containing regions of tensile and compressive stress are consistent with those observed experimentally. In general, the ability of the proposed model to accurately reproduce the measured A-SNOM spectra of various samples irrespective of their stress/strain condition has a number of practical benefits. For example, in the case of a sample with known properties (e.g., a known dielectric function), the simulated spectra provide a convenient means of verifying the correctness of the detection signals obtained from the experimental setup. Meanwhile, for samples in which the properties are unknown, the proposed method provides the means to extract the dielectric function from the measured spectrum. Hence, the proposed method is expected to be of considerable benefit in supporting the on-going development and optimization of new products and processes in the micro- and nano-electromechical systems (MEMS and NEMS) fields.

ACKNOWLEDGMENT

REFERENCES

1. Pohl, D. W., S. Denk, and M. Lanz, "Optical stethoscopy: Image recording with resolution $\lambda/20$," *J. Appl. Phys.*, Vol. 44, 651–653, 1984.
2. Jackson, J. D., *Classical Electrodynamics*, Wiley, 1999.
3. Patane, S., G. G. Gucciardi, M. Labardi, and M. Allegrini, "Apertureless near-field optical microscopy," *Rivita Del Nuovo Cimento*, Vol. 27, 1–46, 2004.

4. Wessel, J., "Surface-enhanced optical microscopy," *J. Opt. Soc. Am.*, Vol. 2, 1538–1540, 1985.

5. Wickramasinghe, H. K. and C. C. Williams, "Apertureless near field optical microscope," US Patent 4 947 034, 1990.

6. Inouye, Y. and S. Kawata, "Near-field scanning optical microscope with a metallic probe tip," *Opt. Lett.*, Vol. 19, 159–161, 1994.

7. Hillenbrand, R. and F. Keilmann, "Complex optical constants on a subwavelength scale," *Phys. Rev. Lett.*, Vol. 85, 3029–3032, 2000.

8. Hillenbrand, R., B. Knoll, and F. Keilmann, "Pure optical contrast in scattering-type scanning near-field microscopy," *J. Microsc.*, Vol. 202, 77–83, 2000.

9. Knoll, B. and F. Keilmann, "Enhanced dielectric contrast in scattering-type scanning near-field optical microscopy," *Opt. Commun.*, Vol. 182, 321–328, 2000.

10. Hudlet, S., S. Aubert, A. Bruyant, R. Bachelot, P. M. Adam, J. L. Bijeon, G. Lerondel, P. Royer, and A. A. Stashkevich, "Apertureless near field optical microscopy: A contribution to the understanding of the signal detected in the presence of background field," *Opt. Commun.*, Vol. 230, 245–251, 2004.

11. Formanek, F., Y. D. Wilde, and L. Aigouy, "Analysis of the measured signals in apertureless near-field optical microscopy," *Ultramicroscopy*, Vol. 103, 133–139, 2005.

12. Gucciardi, P. G., G. Bachelier, and M. Allegrini, "Far-field background suppression in tip-modulated apertureless near-field optical microscopy," *J. Appl. Phys.*, Vol. 99, No. 124309, 2006.

13. Stefanon, I., S. Blaize, A. Bruyant, S. Aubert, G. Lerondel, R. Bachelot, and P. Royer, "Heterodyne detection of guided waves using a scattering-type scanning near-field optical microscope," *Opt. Express*, Vol. 13, 5553–5564, 2005.

14. Chuang, C. H. and Y. L. Lo, "Analytical analysis of modulated signal in apertureless scanning near-field optical microscopy," *Opt. Express*, Vol. 15, 15782–15796, 2007.

15. Chuang, C. H. and Y. L. Lo, "An analysis of heterodyne signals in apertureless scanning near-field optical microscopy," *Opt. Express*, Vol. 16, 17982–18003, 2008.

16. Chuang, C.-H. and Y.-L. Lo, "Signal analysis of apertureless scanning near-field optical microscopy with superlens," *Progress In Electromagnetics Research*, Vol. 109, 83–106, 2010.

17. Cvitkovic, A., N. Ocelic, and R. Hillenbrand, "Analytical model for quantitative prediction of material contrasts in scattering-type near-field optical microscopy," *Opt. Express*, Vol. 15, 8550–8565,

2007.

18. Xie, H., F. M. Kong, and K. Li, "The electric field enhancement and resonance optical antenna composed of AU nanoparicles," *Journal of Electromagnetic Waves and Applications*, Vol. 23, No. 4, 534–547, 2009.

19. Hamid, A.-K. and F. R. Cooray, "Scattering by a perfect electromagnetic conducting elliptic cylinder," *Progress In Electromagnetics Research Letters*, Vol. 10, 59–67, 2009.

20. Mohamed, M. A., E. F. Kuester, M. Piket-May, and C. L. Holloway, "The field of an electric dipole and the polarizability of a conducting object embedded in the interface between dielectric materials," *Progress In Electromagnetics Research B*, Vol. 16, 1–20, 2009.

21. Eroglu, A. and J. K. Lee, "Far field radiation from an arbitrarily oriented hertzian dipole in an unbounded electricaly gyrotropic medium," *Progress In Electromagnetics Research*, Vol. 89, 291–310, 2009.

22. Kalaee, P. and J. Rashed-Mohassel, "Investigation of dipole radiation pattern above a chiral media using 3D bi-FDTD approach," *Journal of Electromagnetic Waves and Applications*, Vol. 23, No. 1, 75–86, 2009.

23. Zhang, S., S.-X. Gong, Y. Guan, J. Ling, and B. Lu, "A new approach for synthesizing both the radiation and scattering patterns of linear dipole antenna array," *Journal of Electromagnetic Waves and Applications*, Vol. 24, No. 7, 861–870, 2010.

24. Laviada-Martinez, J., Y. Alvarez Lopez, and F. Las-Heras, "Efficient determination of the near-field in the vicinity of an antenna for the estimation of its safety perimeter," *Progress In Electromagnetics Research*, Vol. 103, 371–391, 2010.

25. Huber, A. J., A. Ziegler, T. Köck, and R. Hillenbrand, "Infrared nanoscopy of strained semiconductors," *Nature Nanotechnology*, Vol. 4, 153–157, 2008.

26. Aizpurua, J., T. Taubner, F. J. García de Abajo, M. Brehm, and R. Hillenbrand, "Substrate-enhanced infrared near-field spectroscopy," *Opt. Express*, Vol. 16, 1529–1545, 2008.

27. Walford, J. N., J. A. Porto, R. Carminati, J. J. Greffet, P. M. Adam, S. Hudlet, J. L. Bijeon, A. Stashkevich, and P. Royer, "Influence of tip modulation on image formation in scanning near-field optical microscopy," *J. Appl. Phys.*, Vol. 89, 5159–5169, 2001.

28. Gomez, L., R. Bachelot, A. Bouhelier, G. P. Wiederrecht,

S. H. Chang, S. K. Gray, F. Hua, S. Jeon, J. A. Rogers, M. E. Castro, S. Blaize, I. Stefanon, G. Lerondel, and P. Royer, "Apertureless scanning near-field optical microscopy: A comparison between homodyne and heterodyne approaches," *J. Opt. Soc. Am. B*, Vol. 23, 823–833, 2006.

29. Lo, Y. L. and C. H. Chuang, "New synthetic-heterodyne demodulation for an optical fiber interferometry," *IEEE J. Quantum Electro.*, Vol. 37, 658–663, 2001.

30. Bek, A., "Apertureless SNOM: A new tool for nano-optics," Ph.D. Dissertation, Max Planck Institute for Solid State Research, Germany, 2004.

31. Palik, E. D., *Handbook of Optical Constants of Solids*, Academic, New York, 1985.

32. Harima, H., S. Nakashima, and T. Uemura, "Raman-scattering from anisotropic LO-phonon-plasmon-coupled mode in n-type 4H-SiC and 6H-SiC," *J. Appl. Phys.*, Vol. 78, 1996–2005, 1995.

33. Huber, A., N. Ocelic, T. Taubner, and R. Hillenbrand, "Nanoscale resolved infrared probing of crystal structure and of plasmonCphonon coupling," *Nano Lett.*, Vol. 6, 774–778, 2006.

34. Liu, J. and Y. K. Vohra, "Raman modes of 6H polytype of silicon-carbide to ultrahigh pressures — A comparison with silicon and diamond," *Phys. Rev. Lett.*, Vol. 72, 4105–4108, 1994.